



## Effect of strain rate and crystalline inclusions on mechanical properties of bulk glassy and partially crystallized $Zr_{52.5}Cu_{17.9}Ni_{14.6}Al_{10}Ti_5$ alloy

Tomasz KOZIEL<sup>1</sup>, Krzysztof PAJOR<sup>1</sup>, Grzegorz CIOS<sup>2</sup>, Piotr BAŁA<sup>1,2</sup>

1. Faculty of Metals Engineering and Industrial Computer Science,  
AGH University of Science and Technology, Al. Mickiewicza 30, 30-059 Krakow, Poland;

2. Academic Centre for Materials and Nanotechnology,  
AGH University of Science and Technology, Al. Mickiewicza 30, 30-059 Krakow, Poland

Received 25 July 2018; accepted 15 March 2019

**Abstract:** The mechanical properties of the  $Zr_{52.5}Cu_{17.9}Ni_{14.6}Al_{10}Ti_5$  alloy were presented, with an emphasis on the strain rate effect and presence of crystalline inclusions on the deformation and fracture mechanisms. X-ray diffraction studies indicated fully amorphous alloy structures with lower oxygen contents and partial crystalline structures at higher oxygen levels; however, completely different compressive deformation behaviour was observed. Uniaxial compression tests of the fully amorphous alloy showed elastic deformation, followed by yielding, distinct plastic deformation and serration flow behaviour. An increase in strain rate from  $1 \times 10^{-4}$  to  $1 \times 10^{-2} \text{ s}^{-1}$  did not affect the yield strength; however, it decreased the compressive fracture strength and reduced the plastic strain. Scanning electron microscopy (SEM) observations with energy dispersive spectroscopy (EDS) analysis showed that the intermetallic  $CuZr_2$  phase was present even in the low oxygen content alloy, leading to lower fracture strength and ductility loss. For the high oxygen level samples, the presence of the dendritic  $Zr_{51}Cu_{28}Al_{21}$  phase was confirmed, leading to fracture strength impairment. The difference between ductile and brittle samples has been reflected on the fracture surfaces. The higher the plastic strain was, the higher the density of shear bands forming during deformation manifested by a serration flow behaviour on stress–strain curves.

**Key words:** bulk metallic glasses; compression test; shear band; X-ray diffraction

### 1 Introduction

Bulk metallic glasses (BMGs) are solid alloys that exhibit superior properties, compared to their crystalline counterparts, originating from the random arrangement of atoms and lack of classical lattice defects. Substantial attention has been paid to Zr-based BMGs due to their high glass-forming ability at a relatively low cost of constituent elements. It is well known that Zr-based BMGs possess a high elastic limit, high strength and hardness, as well as good corrosion and wear resistance [1–4]. The main drawback of most BMGs is limited macroscopic plasticity, usually below 1% under compression and near zero under tension [5–7]. There are two different mechanisms trying to explain the heterogeneous plasticity of BMGs, i.e. free-volume and shear transformation zone (STZ) models. The former was adapted to BMGs by SPAEPEN [8] and defines the free

volume as the excess atomic volume of an ideally packed reference amorphous state. The free volume model considers deformation as a series of atomic jumps, which is, in fact, a diffusion-like process, at sites with a high density of free volumes. The STZ model was proposed by ARGON [9] and further improved by FALK and LANGER [10]. Here, the plastic strain is produced by the cooperative movement of numerous atoms under an applied stress and with the assistance of thermal fluctuations in regions around the free-volume sites. Nevertheless, both mechanisms assume that local atom rearrangement can accommodate shear strain and that the plastic deformation of BMGs at room temperature is highly localised within narrow regions called shear bands (SBs). The appearance of new SBs during compression is manifested by serrations in the stress–strain curve at a constant crosshead speed. Serration is characterised by repeating sudden stress drops and small displacement burst cycles during plastic deformation. Single serration

can be associated with the operation of several SBs [11]. There are two types of serration dynamics in BMGs, namely chaotic and self-organized critical (SOC). SOC behaviour is observed in “ductile” BMGs, caused by the nucleation and propagation of numeral SBs and their interactions [12–14]. The rate of nucleation and propagation of SBs should be consistent with the applied strain rates. If the loading rate is too fast, the emission/propagation rate of the SBs is not sufficient enough to accommodate the strain, which leads to early fracture. SONG et al [15] have estimated the critical strain rate at  $1 \times 10^{-5} \text{ s}^{-1}$  for the  $\text{Zr}_{56}\text{Al}_{10.9}\text{Ni}_{4.6}\text{Cu}_{27.8}\text{Nb}_{0.7}$  bulk glassy alloy, enabling the highest fracture strength and plastic strain. Therefore, depending on the strain rate, negative or positive strain rate dependence can be observed. A slight decrease in fracture strength (negative strain rate dependence) is observed up until reaching the critical strain rate, while for high strain rates an opposite relation can be found [11,15]. Moreover, an increase in strain rate decreases the plastic strain [16,17].

The ductility of BMGs can be improved by the presence of secondary phases dispersed in the amorphous matrix. This may hinder the propagation of the shear bands and dissipate fracture energy [18,19]. HAYS et al [20] showed that the ductility of  $\text{Zr}_{41.2}\text{Ti}_{13.8}\text{Cu}_{12.5}\text{Ni}_{10}\text{Be}_{22.5}$  BMG can be significantly improved via partial crystallisation of the dendritic  $\beta\text{-Ti-Zr-Nb}$  phase. However, the effect of the secondary phase strongly depends on the type, volume fraction, shape and size of the reinforcing particles. In fact, the existence of a ductile phase is not sufficient for improving plastic deformation. An effective interaction is necessary between the microstructural length scale of the reinforcing particles and critical mechanical length scales (shear band width and spacing) [21]. YOKOYAMA et al [22] showed that the presence of crystalline inclusions, related to oxygen content, caused fatal drawbacks in the mechanical properties of BMGs. Oxygen impurities are considered to be the most detrimental factors leading to the deterioration of the glass-forming ability and mechanical properties of Zr-based systems by triggering the heterogeneous nucleation in undercooled melt [23]. LIN et al [24] showed that an increase in oxygen contents from  $250 \times 10^{-6}$  to  $5250 \times 10^{-6}$  (mass fraction, the same below if not mentioned) in the  $\text{Zr}_{52.5}\text{Cu}_{17.9}\text{Ni}_{14.6}\text{Al}_{10}\text{Ti}_5$  alloy leads to a decrease in crystallisation time at a given temperature by orders of magnitude. Thus, the synthesis of BMGs requires using high purity elements and strict casting conditions. KERYVIN [25] reported that oxygen concentrations lower than  $300 \times 10^{-6}$  (mole fraction) are very unlikely to be reached, even for the highest purity Zr and good casting conditions.

This work, presents structures and mechanical

properties of the suction-cast  $\text{Zr}_{52.5}\text{Cu}_{17.9}\text{Ni}_{14.6}\text{Al}_{10}\text{Ti}_5$  alloy, synthesised using two different forms and purities of Zr metal. The effect of strain rate on mechanical properties is linked to the structure type (amorphous or partially crystalline) and applied cooling rates (rods of different diameters).

## 2 Experimental

The  $\text{Zr}_{52.5}\text{Cu}_{17.9}\text{Ni}_{14.6}\text{Al}_{10}\text{Ti}_5$  alloy (commercially known as Vitreloy 105) was prepared via arc melting of high purity elements: Cu 99.99%, Ni 99.9%, Al 99.999%, Ti 99.9% and two types of Zr metal with different oxygen contents:  $150 \times 10^{-6}$  (Zr crystal bar, 99.95%) and  $1200 \times 10^{-6}$  (Zr rod, 99.8%). The Zr rod included 2.1% Hf, as both elements exhibit chemical similarities. In the case of the Zr crystal bar, obtained via the iodide process, the nominal Hf content was below  $150 \times 10^{-6}$ .

The alloy was suction-cast into  $d3$  and  $d5$  mm cylindrical cavity copper moulds. The minimum axial cooling rates were determined as about 200 K/s for  $d3$  mm and 30 K/s for  $d5$  mm rods [26]. As the Zr metals and, consequently, the suction-cast alloys contain different amounts of oxygen, the samples are referred to as low oxygen (LO) and high oxygen (HO).

The structures of the as-cast rods were analyzed using X-ray diffraction with  $\text{Cu K}_\alpha$  radiation (Panalytical Empyrean). Standard grinding and polishing procedures (final polishing with colloidal silica suspension) were applied to revealing any possible microstructural heterogeneities by means of scanning electron microscopy (FEI Versa 3D) using back-scattered electron (BSE) and EDS detectors. This microscope was also used for fracture surface observations after compression tests using a secondary electron (SE) detector.

Room temperature uniaxial compressive tests (Instron 5982) were carried out by applying different initial strain rates:  $1 \times 10^{-2}$ ,  $1 \times 10^{-3}$  and  $1 \times 10^{-4} \text{ s}^{-1}$ . At least 3 specimens were tested at each strain rate. The height-to-diameter aspect ratio of the bulk compression specimens was kept to 1.5:1 and both ends of the specimens were carefully ground to make them parallel. The Vickers hardness measurements were performed under a load of 9.81 N.

The oxygen contents were analysed via the inert gas fusion method using LECO ON 736 with a Ni basket and  $\sim 0.05 \text{ g}$  graphite powder. An average of three measurements was taken for each variant.

## 3 Results and discussion

### 3.1 Structure characterization

The mean oxygen contents of the as-cast rod samples, synthesised using a Zr crystal bar and rod, were

measured to be  $(183\pm 6)\times 10^{-6}$  (LO) and  $(1000\pm 10)\times 10^{-6}$  (HO), respectively. These values correspond to  $(833\pm 27)\times 10^{-6}$  (mole fraction,  $\sim 0.08$  at.%) and  $(4538\pm 45)\times 10^{-6}$  (mole fraction,  $\sim 0.45$  at.%) of oxygen.

The XRD patterns (Fig. 1) of the LO samples indicate fully amorphous structures, based on the presence of a broad diffraction halo. For the HO alloy and lower cooling rate sample ( $d5$  mm), two crystalline peaks were superimposed on the amorphous diffraction halo. These peaks most probably correspond to the tetragonal  $\text{CuZr}_2$  phase.

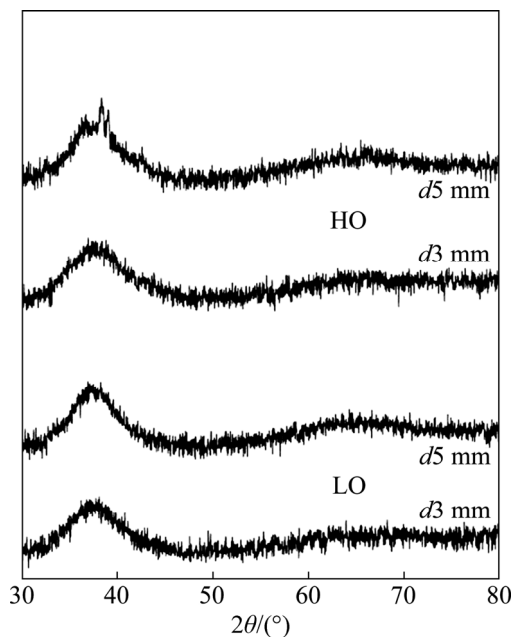


Fig. 1 XRD patterns of studied alloy cast into  $d3$  and  $d5$  mm rods with low oxygen (LO) and high oxygen (HO) content

Figure 2 shows the cross-sectional SEM images of the LO alloy, cast into  $d3$  and  $d5$  mm rods. Several samples of each variant underwent this analysis. No crystallinity was observed (within the resolution of the microscope) for samples from the cast LO  $d3$  mm rod (Figs. 2(a, b)). For samples from the  $d5$  mm rod, some areas containing crystalline precipitates were observed (Fig. 2(d)), but, not in all studied samples. This means that partial crystallisation occurred for higher diameter samples, although the crystallite volume fraction was below the detection limit of XRD. Energy-dispersive spectroscopy (EDS) analysis (not shown here) did not reveal any compositional differences between the matrix and precipitates.

SEM micrographs of the HO sample showed the presence of crystalline phases embedded within the amorphous matrix. A typical crystalline inclusion array, related to the oxygen contents, can be observed for the  $d3$  mm samples (Fig. 3). YOKOYAMA et al [22] reported that this kind of morphology is related to the thermal convection in the molten alloy and the inclusions formed on the oxidised surface. A detailed EDS elemental map (Fig. 4) of this sample showed that the dendrites were enriched with Al at the expense of Ni, while Zr, Cu and Ti distribute the same as in the matrix. Additionally, a higher oxygen contrast can be found in the dendrites, indicating that their formation was induced by a high oxygen level. Based on the EDS analysis, the chemical composition of the crystalline inclusions was determined to be  $\text{Zr}_{49.1}\text{Cu}_{15.7}\text{Ni}_9\text{Al}_{21.4}\text{Ti}_{3.4}$ , which is close to the composition of the  $\text{Zr}_{51}\text{Cu}_{28}\text{Al}_{21}$  ( $\tau_3$ ) phase. This type of inclusion has already been observed in other Zr-based BMGs [22,27].

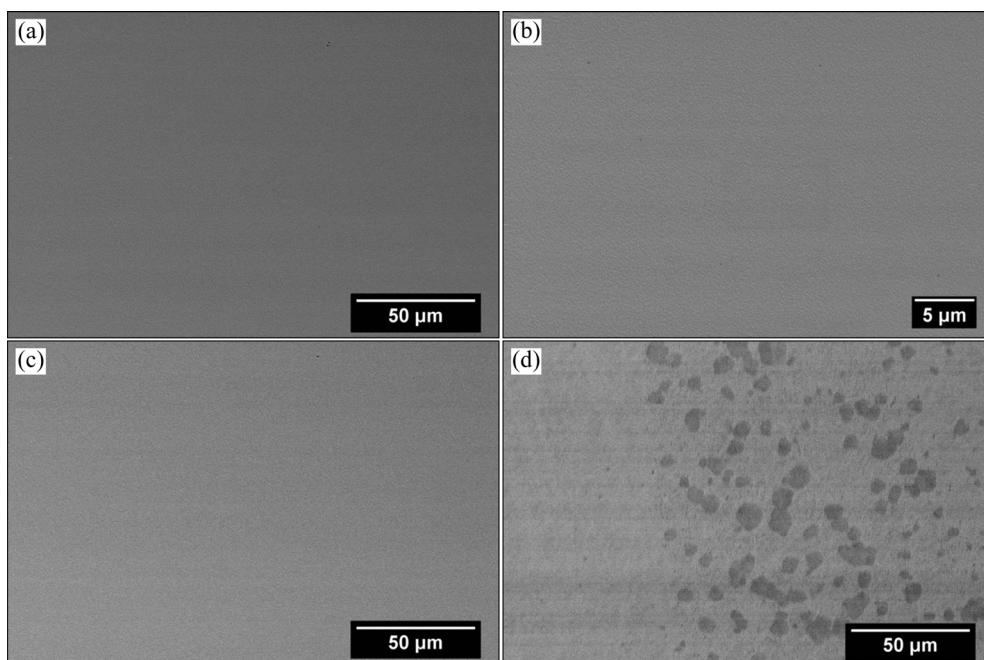


Fig. 2 SEM-BSE images of  $d3$  mm (a, b) and  $d5$  mm (c, d) LO suction-cast rods

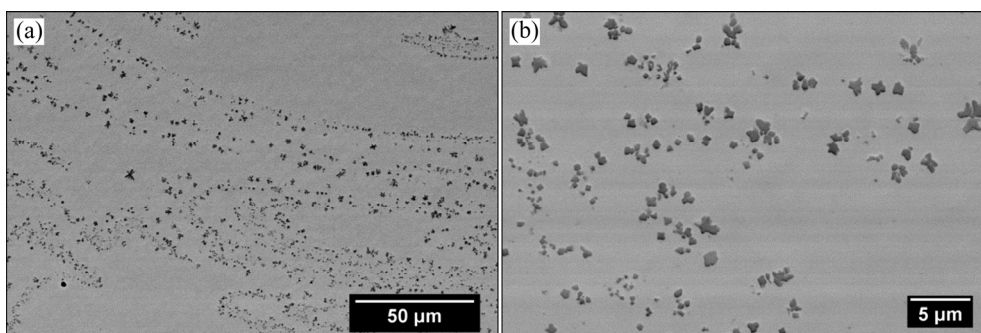


Fig. 3 SEM-BSE images of  $d3$  mm HO suction-cast rod

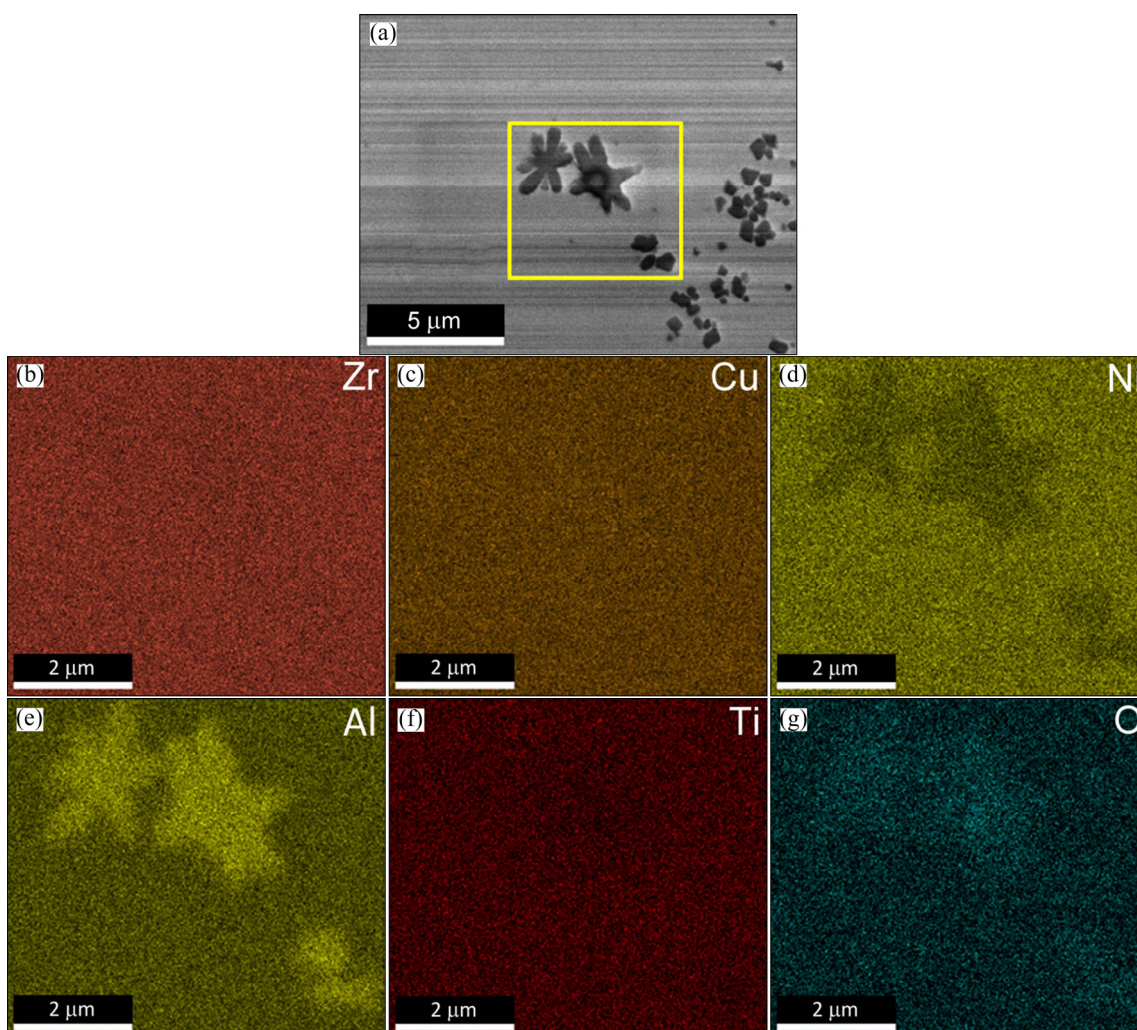


Fig. 4 SEM image (a) and EDS elemental distribution maps (b–g) of  $d3$  mm HO suction-cast rod

SEM images of the  $d5$  mm HO suction-cast  $Zr_{52.5}Cu_{17.9}Ni_{14.6}Al_{10}Ti_5$  alloy are presented in Fig. 5. A significantly lower cooling rate for  $d5$  mm suction-cast samples than for  $d3$  mm samples (30 vs. 200 K/s), besides a typical crystalline inclusion array brought about large crystallites with size between 20 and 50  $\mu m$ . EDS mapping (Fig. 6) proved that the crystalline inclusions (dendritic phase) were enriched with Al and oxygen, as in the case of the lower diameter sample. However, no compositional differences between the

matrix and the big crystallites (dark grey contrast phase) were detected within the SEM resolution. This means that the big crystallites could be formed by a massive transformation upon cooling from the melt, in which the product phase has a different structure but the same composition as the surrounding matrix. Based on the chemical composition, it was assumed that this phase is most probably the  $CuZr_2$  tetragonal phase, which was confirmed to crystallise polymorphically from the glassy matrix upon heating [28].

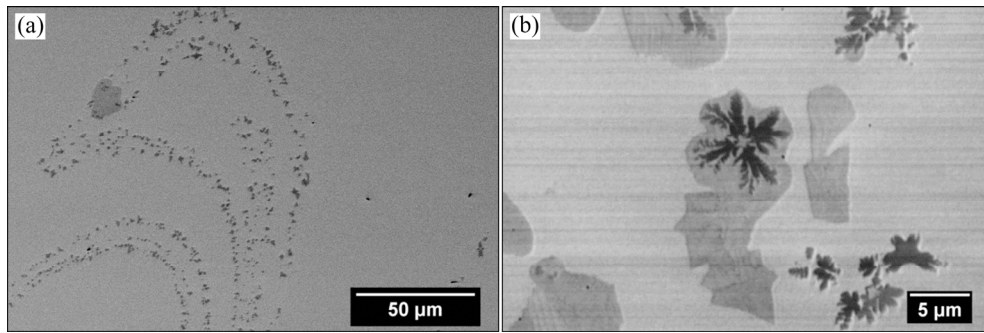


Fig. 5 SEM-BSE images of *d*5 mm HO suction-cast rod

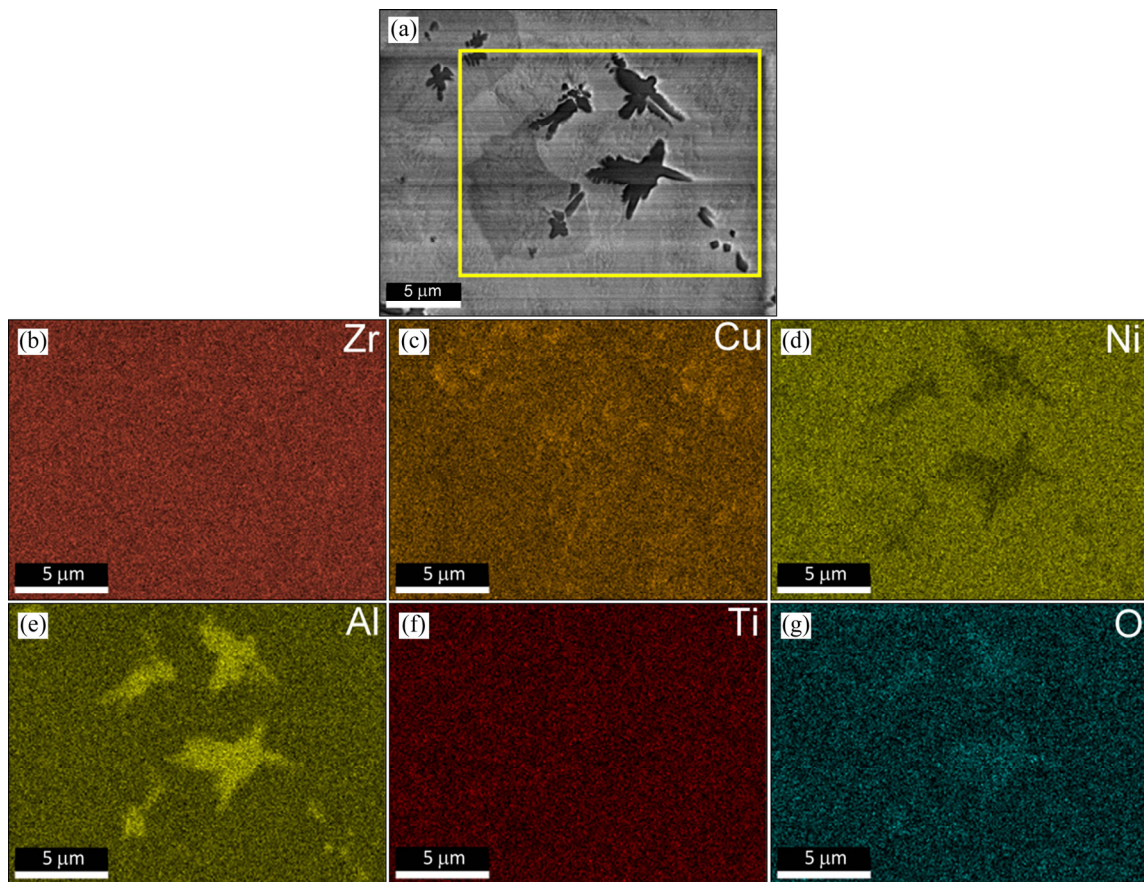
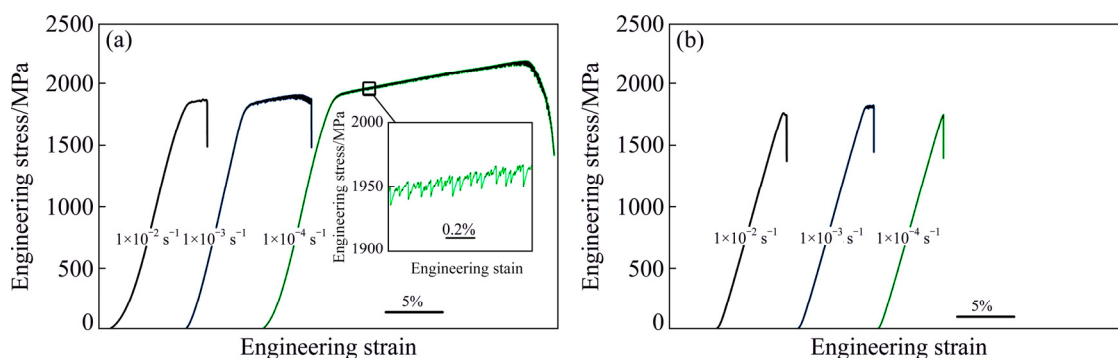


Fig. 6 SEM image (a) and EDS elemental distribution maps (b–g) of *d*5 mm HO suction-cast rod

### 3.2 Compressive deformation behaviour

Figures 7 and 8 show the engineering stress–strain curves of the  $Zr_{52.5}Cu_{17.9}Ni_{14.6}Al_{10}Ti_5$  alloy under compression. Mechanical properties, including the compressive yield strength ( $\sigma_y$ ), compressive fracture strength ( $\sigma_f$ ) and plastic strain ( $\epsilon_{pl}$ ), together with Vickers hardness, are summarized in Table 1. A similar hardness level (HV1  $\sim$ 530) was measured with different oxygen levels; however, their compressive behaviours were completely different. The stress–strain curves of the *d*3 mm LO samples (Fig. 7(a)) were characterised by elastic deformation, followed by yielding and serrated plastic deformation before fracture failure. An increase in strain

rate from  $1 \times 10^{-4}$  to  $1 \times 10^{-2} \text{ s}^{-1}$  did not change the compressive yield strength ( $\sigma_y \sim 1790 \text{ MPa}$ ); however, negative strain rate dependence was noticed for the compressive fracture strength, as the  $\sigma_f$  decreased from  $\sim 2160$  to  $\sim 1900 \text{ MPa}$  for the highest strain rate. This effect was attributed to the extent of serration flow behaviour caused by different strain rates, as the lower loading rate enabled the activation and propagation of new SBs that can accommodate the strain. Thus, the highest plastic strain of 16.7% was observed for the lowest strain rate. The serration flow behaviour (inset in Fig. 7(a)) represents SOC dynamics, corresponding to the nucleation and interaction of a large number of SBs.



**Fig. 7** Compressive stress–strain curves of LO alloy samples: (a)  $d3$  mm $\times$ 4.5 mm; (b)  $d5$  mm $\times$ 7.5 mm (The curves are shifted relative to each other for clarity)

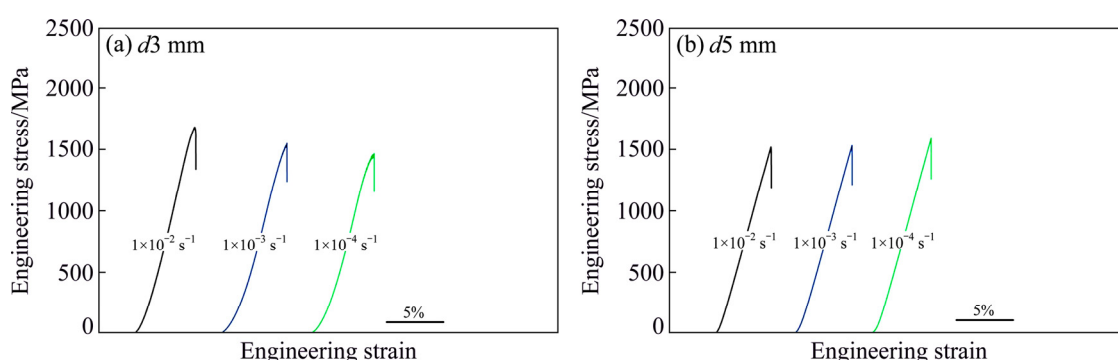


**Fig. 8** Compressive stress–strain curves of HO alloy samples: (a)  $d3$  mm $\times$ 4.5 mm; (b)  $d5$  mm $\times$ 7.5 mm (The curves are shifted relative to each other for clarity)

**Table 1** Mechanical properties of  $Zr_{52.5}Cu_{17.9}Ni_{14.6}Al_{10}Ti_5$  alloy subjected to compression tests and Vickers hardness measurements of as-cast samples

Oxygen level	Rod diameter/mm	Strain rate/s <sup>-1</sup>	$\sigma_y$ /MPa	$\sigma_f$ /MPa	$\epsilon_{pl}/\%$	Vickers hardness (HV1)
LO	3	$1 \times 10^{-2}$	1792 $\pm$ 82	1903 $\pm$ 26	4.0 $\pm$ 2.7	
		$1 \times 10^{-3}$	1792 $\pm$ 55	1898 $\pm$ 48	4.7 $\pm$ 1.2	529 $\pm$ 4
		$1 \times 10^{-4}$	1790 $\pm$ 77	2166 $\pm$ 36	16.7 $\pm$ 2.7	
	5	$1 \times 10^{-2}$	1765 $\pm$ 0	1772 $\pm$ 7	0.3 $\pm$ 0.1	
		$1 \times 10^{-3}$	–	1808 $\pm$ 35	–	530 $\pm$ 5
		$1 \times 10^{-4}$	–	1749 $\pm$ 40	–	
HO	3	$1 \times 10^{-2}$	–	1758 $\pm$ 97	–	
		$1 \times 10^{-3}$	–	1623 $\pm$ 115	–	530 $\pm$ 6
		$1 \times 10^{-4}$	–	1550 $\pm$ 133	–	
	5	$1 \times 10^{-2}$	–	1501 $\pm$ 90	–	
		$1 \times 10^{-3}$	–	1604 $\pm$ 68	–	536 $\pm$ 8
		$1 \times 10^{-4}$	–	1549 $\pm$ 164	–	

A pronounced ductility of the fully amorphous  $Zr_{52.5}Cu_{17.9}Ni_{14.6}Al_{10}Ti_5$  alloy is related to a high Poisson ratio, which indicates the tendency for plastic or brittle failure and depends on the nature of the atomic bonding in the metallic glass. It is argued that the macroscopic

plastic deformability of bulk glassy alloy significantly increases if the Poisson ratio exceeds 0.31–0.32 [29,30] and this value was estimated to be as high as 0.371 for the studied alloy [31].

In contrast, no distinct plastic strain was observed

for the higher diameter (5 mm) samples with the same oxygen level (Fig. 7(b)), and the fracture stress corresponded to the yield strength of the smaller diameter samples. One possible explanation of such a dramatic change is a decrease in cooling rate during solidification, leading to lower amounts of free volumes that are known to facilitate the plastic deformation in BMGs [32]. However, an increase in sample diameter from 3 to 5 mm resulted in a partial crystallisation of the intermetallic  $\text{CuZr}_2$  phase, and the presence of this phase is considered to be a major deleterious factor affecting mechanical properties of the low oxygen alloy.

Figure 8 shows stress–strain curves for the  $\text{Zr}_{52.5}\text{Cu}_{17.9}\text{Ni}_{14.6}\text{Al}_{10}\text{Ti}_5$  alloy with high oxygen contents. The samples fractured at low strength levels and without any plastic deformation, even for the lowest strain rate. No distinct differences between 3 and 5 mm diameter samples were noticed, which means that the presence of the crystalline dendritic inclusions ( $\tau_3$  phase) further impaired mechanical properties.

The detrimental effect of the crystalline phases on the mechanical properties of alloy must be related to their brittle nature. INOUE et al [22,33] reported that the presence of  $\text{CuZr}_2$  or  $\tau_3$  phases in Zr-based alloys causes embrittlement.

### 3.3 Fractography

SEM images of the fracture morphologies and magnified images of rod surfaces are shown in Figs. 9 and 10. The fracture surfaces of the fully amorphous

(low oxygen,  $d3$  mm) samples contained typical vein-like patterns (Figs. 9(a, b)); however, some smooth regions could also be seen. Multiple shear bands were observed on the lateral outer surfaces of the fractured samples and the density of SBs was the highest for the lowest strain rate (insets in Figs. 9(a and b)), indicating larger plastic deformation. In contrast, only a few SBs could be observed on the surface of the higher diameter sample (inset in Fig. 9(c)), where a river-like patterns could additionally be seen (Fig. 9(d)). The ductile to brittle transition could also be indicated by the clearly visible re-solidified droplet features, marked by arrows in Fig. 9(d).

Similar fracture surfaces were observed for the HO samples (Fig. 10). However, for these samples, crystalline  $\tau_3$  inclusions were observed, the residual melting pattern was more pronounced. In some regions of the  $d5$  mm samples, re-solidified spreading liquid zones were observed on the fracture surface layers (Fig. 10(c)). This phenomenon is related to the dissipation of elastic strain energy stored within a few shear bands at the final failure and is often accompanied by light emission [34]. Only single shear bands could be observed on the lateral outer surfaces (insets in Figs. 10(a, b, c)), as the samples fractured without distinct plastic strain. This means that the difference between ductile and brittle fracture mode is manifested by shear band formation. The greater the plasticity is, the higher the density of closely spaced shear bands is.

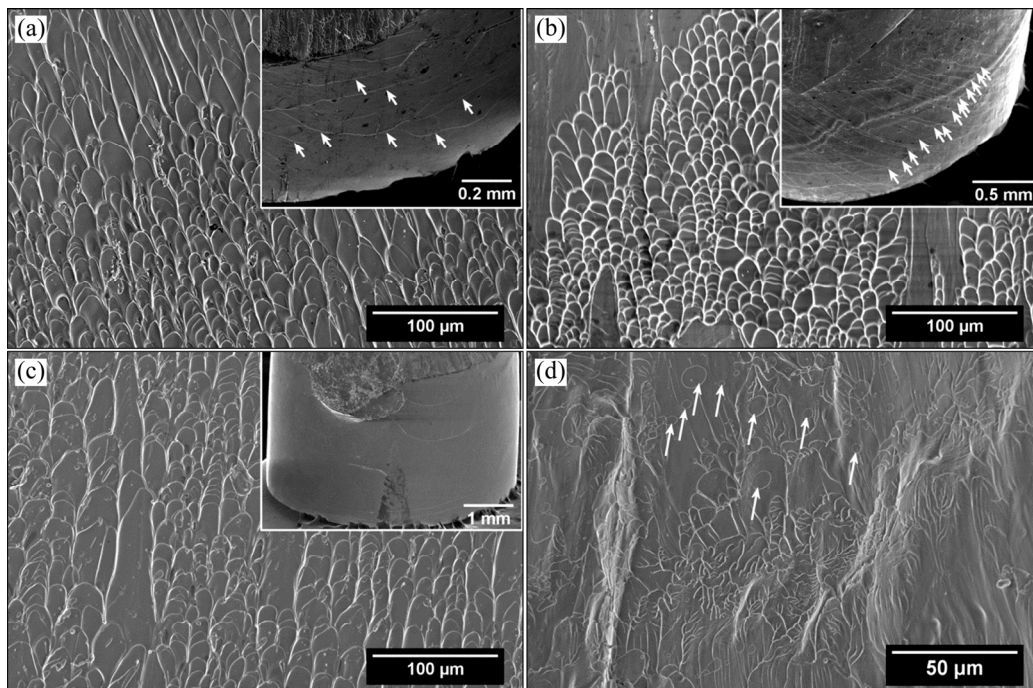


**Fig. 9** SEM micrographs of fracture surfaces of  $\text{Zr}_{52.5}\text{Cu}_{17.9}\text{Ni}_{14.6}\text{Al}_{10}\text{Ti}_5$  alloy with LO contents, after compressive deformation: (a)  $d3$  mm,  $\dot{\epsilon}=1\times 10^{-2}$  s $^{-1}$ ; (b)  $d3$  mm,  $\dot{\epsilon}=1\times 10^{-4}$  s $^{-1}$ ; (c, d)  $d5$  mm,  $\dot{\epsilon}=1\times 10^{-4}$  s $^{-1}$  (Insets show magnified images of lateral surfaces)

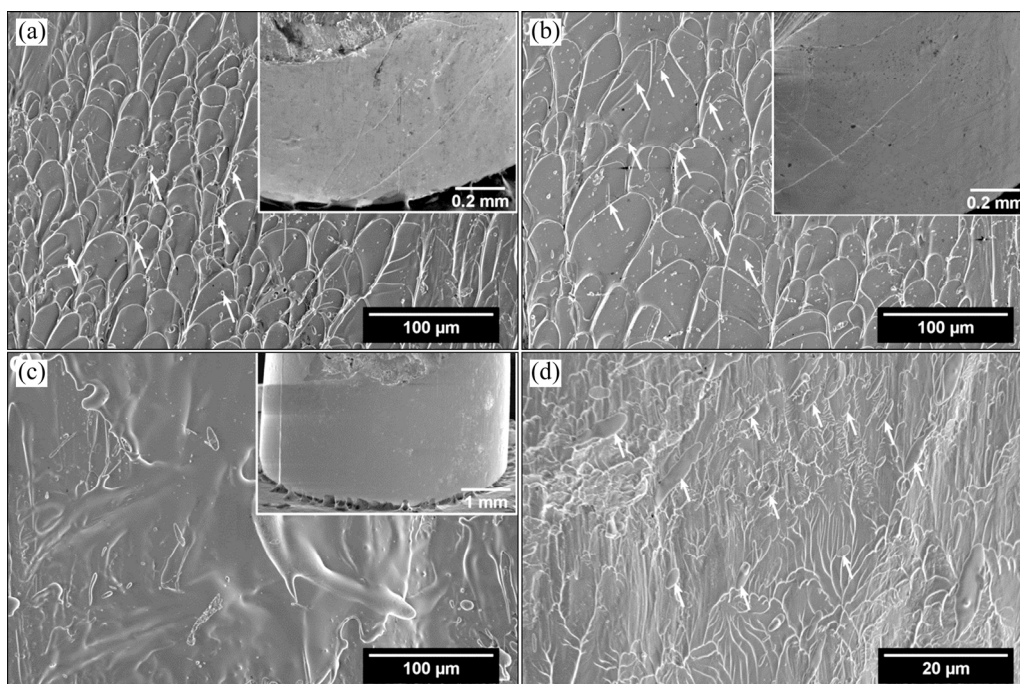


**Fig. 10** SEM micrographs of fracture surfaces of  $Zr_{52.5}Cu_{17.9}Ni_{14.6}Al_{10}Ti_5$  alloy with HO contents, after compressive deformation: (a)  $d3$  mm,  $\dot{\epsilon}=1\times 10^{-2}$  s $^{-1}$ ; (b)  $d3$  mm,  $\dot{\epsilon}=1\times 10^{-4}$  s $^{-1}$ ; (c, d)  $d5$  mm,  $\dot{\epsilon}=1\times 10^{-4}$  s $^{-1}$  (Insets show magnified images of lateral surfaces)

## 4 Conclusions

(1) Two oxygen levels were obtained in the  $Zr_{52.5}Cu_{17.9}Ni_{14.6}Al_{10}Ti_5$  alloy via synthesis of high purity elements, including different forms of Zr and various oxygen contents.

(2) Despite the alloys possessing similar hardness values, a significant difference in compressive deformation behaviour was observed between the fully amorphous and partially crystallized samples. Low oxygen contents ( $\sim 180\times 10^{-6}$ ) enabled the formation of an amorphous structure in suction-cast  $d3$  mm samples, characterised by high fracture strength (over 2100 MPa) and 16% of plastic strain under compression at a strain rate of  $1\times 10^{-4}$  s $^{-1}$ .

(3) An increase in strain rate reduced the plastic strain as the shear bands could not accommodate the imposed strain fast enough. The formation of shear bands was manifested by a serration flow on the stress–strain curve and a density of shear bands on the lateral outer surfaces.

(4) Any trace of crystalline phase embedded in the amorphous matrix of the  $Zr_{52.5}Cu_{17.9}Ni_{14.6}Al_{10}Ti_5$  alloy severely deteriorates mechanical properties. Two crystalline phases were observed, i.e.  $CuZr_2$ , due to insufficient cooling rate, and dendritic  $Zr_{51}Cu_{28}Al_{21}$  ( $\tau_3$ ) crystalline inclusions, related to high oxygen contents.

Their presence led to loss in ductility, even for the lowest strain rate.

## Acknowledgments

The research is supported by Ministry of Science and Higher Education Republic of Poland under contract No. 11.11.110.299.

## References

- [1] INOUE A, TAKEUCHI A. Recent development and application products of bulk glassy alloys [J]. *Acta Materialia*, 2011, 59: 2243–2267.
- [2] SUN Y J, QU D D, HUANG Y J, LISS K D, WEI X S, XING D W, SHEN J. Zr–Cu–Ni–Al bulk metallic glasses with superhigh glass-forming ability [J]. *Acta Materialia*, 2009, 57: 1290–1299.
- [3] ZHOU K, LIU Y, PANG S, ZHANG T. Formation and properties of centimeter-size Zr–Ti–Cu–Al–Y bulk metallic glasses as potential biomaterials [J]. *Journal of Alloys and Compounds*, 2016, 656: 389–394.
- [4] BORJA C E, FIGUEROA I A, LOZADA-FLORES O, ESTRADA M, LARA-RODRIGUEZ G A, VERDUZCO J A. Glass formation, thermal and mechanical properties of ZrCuAlNi bulk metallic glasses [J]. *Transactions of Nonferrous Metals Society of China*, 2018, 28: 1157–1165.
- [5] ASHBY M F, GREER A L. Metallic glasses as structural materials [J]. *Scripta Materialia*, 2006, 54: 321–326.
- [6] SARMAH R, ANANTHAKRISHNA G, SUN B A, WANG W H. Hidden order in serrated flow of metallic glasses [J]. *Acta Materialia*,

- 2011, 598: 4482–4493.
- [7] CAI An-hui, LIU Yong, WU Hong, DING Da-wei, AN Wei-ke, ZHOU Guo-jun, LUO Yun, PENG Yong-yi, LI Xiao-song. Effects of aspect ratio and loading rate on room-temperature mechanical properties of Cu-based bulk metallic glasses [J]. Transactions of Nonferrous Metals Society of China, 2016, 26: 2617–2632.
- [8] SPAEPEN F. A microscopic mechanism for steady state inhomogeneous flow in metallic glasses [J]. Acta Metallurgica, 1977, 25: 407–415.
- [9] ARGON A. Plastic deformation in metallic glasses [J]. Acta Metallurgica, 1979, 27: 47–58.
- [10] FALK M L, LANGER J S. Dynamics of viscoplastic deformation in amorphous solids [J]. Physical Review, 1998, 57: 7192–7205.
- [11] DUBACH A, DALLA TORRE F H, LÖFFLER J F. Constitutive model for inhomogeneous flow in bulk metallic glasses [J]. Acta Materialia, 2009, 57: 881–892.
- [12] SARMAH R, ANANTHAKRISHNA G, SUN B A, WANG W H. Hidden order in serrated flow of metallic glasses [J]. Acta Materialia, 2011, 59: 4482–4493.
- [13] WANG G, CHAN K C, XIA L, YU P, SHEN J, WANG W H. Self-organized intermittent plastic flow in bulk metallic glasses [J]. Acta Materialia, 2009, 57: 6146–6155.
- [14] SUN B A, YU H B, JIAO W, BAI H Y, ZHAO D Q, WANG W H. Plasticity of ductile metallic glasses: A self-organized critical state [J]. Physical Review Letters, 2010, 105: 035501.
- [15] SONG M, LI Y, HE Y. Effect of strain rate on the compressive behaviour of a  $Zr_{56}Al_{10.9}Ni_{4.6}Cu_{27.8}Nb_{0.7}$  bulk metallic glass [J]. Philosophical Magazine Letters, 2010, 90: 763–770.
- [16] MA W, KOU H, LI J, CHANG H, ZHOU L. Effect of strain rate on compressive behavior of Ti-based bulk metallic glass at room temperature [J]. Journal of Alloys and Compounds, 2009, 472: 214–218.
- [17] ZHANG J, PARK J M, KIM D H, KIM H S. Effect of strain rate on compressive behavior of  $Ti_{45}Zr_{16}Ni_9Cu_{10}Be_{20}$  bulk metallic glass [J]. Materials Science and Engineering A, 2007, 449–451: 290–294.
- [18] ZHU Z W, ZHENG S J, ZHANG H F, DING B Z, HU Z Q, LIAW P K, WANG Y D, REN Y. Plasticity of bulk metallic glasses improved by controlling the solidification condition [J]. Journal of Materials Research, 2008, 23: 941–948.
- [19] FERRY M, LAWS K J, WHITE C, MISKOVIC D M, SHAMLAYE K F, XU W, BILETSKA O. Recent developments in ductile bulk metallic glass composites [J]. MRS Communications, 2013, 3: 1–12.
- [20] HAYS C C, KIM C P, JOHNSON W L. Microstructure controlled shear band pattern formation and enhanced plasticity of bulk metallic glasses containing in situ formed ductile phase dendrite dispersions [J]. Physical Review Letters, 2000, 84: 2901–2904.
- [21] KÜHN U, ECKERT J, MATTERN N, SCHULTZ L. Microstructure and mechanical properties of slowly cooled Zr–Nb–Cu–Ni–Al composites with ductile bcc phase [J]. Materials Science and Engineering A, 2004, 375–377: 322–326.
- [22] YOKOYAMA Y, SHINOHARA T, FUKAURA K, INOUE A. Characterization of crystalline inclusions in cast bulk Zr–Cu–Ni–Al glassy alloy [J]. Materials Transactions, 2004, 45: 1819–1823.
- [23] WANG W H. Roles of minor additions in formation and properties of bulk metallic glasses [J]. Progress in Materials Science, 2007, 52: 540–596.
- [24] LIN X H, JOHNSON W L, RHIM W K. Effect of oxygen impurity on crystallization of an undercooled bulk glass forming Zr–Ti–Cu–Ni–Al alloy [J]. Materials Transactions, JIM, 1997, 38: 473–477.
- [25] KERYVIN V. Oxygen influence on the mechanical properties of Zr-based bulk metallic glasses [C]//FAN C. The world of bulk metallic glasses and their composites. Trivandrum: Research Signpost, 2007: 1–12.
- [26] KOZIEŁ T. Estimation of cooling rates in suction casting and copper-mould casting processes [J]. Archives of Metallurgy and Materials, 2015, 60: 767–771.
- [27] PAJOR K, KOZIEŁ T, CIOS G, BŁYSKUN P, BAŁA P, ZIELIŃSKA-LIPIEC A. Glass forming ability of the  $Zr_{50}Cu_{40}Al_{10}$  alloy with two oxygen levels [J]. Journal of Non-Crystalline Solids, 2018, 496: 42–47.
- [28] ALTOUNIAN Z, GUO-HUA T, STRÖM-OLSEN J O, MUIR W B. Crystallization of amorphous  $CuZr_2$  [J]. Physical Review B, 1981, 24: 505–509.
- [29] LEWANDOWSKI J J, WANG W H, GREER A L. Intrinsic plasticity or brittleness of metallic glasses [J]. Philosophical Magazine Letters, 2005, 85: 77–87.
- [30] GU X J, MCDERMOTT A G, POON S J, SHIFLET G J. Critical Poisson's ratio for plasticity in Fe–Mo–C–B–Ln bulk amorphous steel [J]. Applied Physics Letters, 2006, 88: 1–3.
- [31] BIAN Z, PAN M X, ZHANG Y, WANG W H. Carbon-nanotube-reinforced  $Zr_{52.5}Cu_{17.9}Ni_{14.6}Al_{10}Ti_5$  bulk metallic glass composites [J]. Applied Physics Letters, 2002, 81: 4739–4741.
- [32] HUANG Y J, SHEN J, SUN J F. Bulk metallic glasses: Smaller is softer [J]. Applied Physics Letters, 2007, 90: 1–4.
- [33] SEKI I, LOUZGUINE-LUZGIN D V, INOUE A. Crystallization and embrittlement behavior of a  $Zr_{55}Al_{10}Ni_5Cu_{30}$  metallic glass having different Si and O contents [J]. Materials Transactions, 2007, 48: 821–825.
- [34] LIU C T, HEATHERLY L, EASTON D S, CARMICHAEL C A, SCHNEIBEL J H, CHEN C H, WRIGHT J L, YOO M H, HORTON J A, INOUE A. Test environments and mechanical properties of Zr-base bulk amorphous alloys [J]. Metallurgical and Materials Transactions A, 1998, 29: 1811–1820.

# 应变速率和晶体包裹体对大块非晶和部分结晶的 $Zr_{52.5}Cu_{17.9}Ni_{14.6}Al_{10}Ti_5$ 合金力学性能的影响

Tomasz KOZIEL<sup>1</sup>, Krzysztof PAJOR<sup>1</sup>, Grzegorz CIOS<sup>2</sup>, Piotr BAŁA<sup>1,2</sup>

1. Faculty of Metals Engineering and Industrial Computer Science,  
AGH University of Science and Technology, Al. Mickiewicza 30, 30-059 Krakow, Poland;

2. Academic Centre for Materials and Nanotechnology,  
AGH University of Science and Technology, Al. Mickiewicza 30, 30-059 Krakow, Poland

**摘要:** 研究  $Zr_{52.5}Cu_{17.9}Ni_{14.6}Al_{10}Ti_5$  合金的力学性能, 着重研究应变速率和晶体包裹体对合金变形和断裂机制的影响。X 射线衍射分析表明, 低氧含量时形成完全非晶态的合金组织, 而当氧含量较高时, 形成部分晶化组织; 但是观察到完全不同的压缩变形行为。单轴压缩试验表明, 全非晶合金具有弹性变形、屈服、明显塑性变形和锯齿流变行为。当应变速率从  $1 \times 10^{-4} s^{-1}$  增加到  $1 \times 10^{-2} s^{-1}$  时, 屈服强度没有变化, 然而, 压缩断裂强度和塑性应力均降低。扫描电镜(SEM) 和能谱(EDS)分析表明, 即使在低氧含量的合金中, 依然存在金属间化合物相  $CuZr_2$ , 从而降低了合金的断裂强度和韧性。结果还证实, 在高氧含量的样品中存在枝晶状的  $Zr_{51}Cu_{28}Al_{21}$  相, 会进一步降低其断裂强度。在断口表面可观察到韧性试样和脆性试样之间的差异。塑性应变越大, 变形过程中形成的剪切带的密度越高, 表现为应力-应变曲线上的锯齿流变行为。

**关键词:** 大块金属玻璃; 压缩试验; 剪切带; X 射线衍射分析

(Edited by Xiang-qun LI)